**Quantifying the Effect of Mutual Coupling in
Ultra-Wideband-Multi-Band Multiple Input Multiple Output
Systems**

A Thesis

Submitted to the Faculty

of

Drexel University

by

Rocco Vincent Dragone Jr.

in partial fulfillment of the

requirements for the degree

of

Master of Science in Electrical Engineering

June 2008

Dedications

This thesis is dedicated to my mom and dad whose love and support made all of this possible.

Acknowledgments

I would like to thank all the faculty at Drexel University who helped me along my academic career here. I would like to especially thank Dr. Kapil R. Dandekar for his wealth of knowledge and tolerance of my constant complaints. If I had never met you, I probably would not be getting a graduate degree.

I would also like to thank all of my lab mates at Drexel University Wireless Systems Lab (and Elaine) for their constant help and advice, and for helping to make the lab a fun place to work in. I really could not have done this without you guys.

Table of Contents

List of Tables

List of Figures

Abstract
Quantifying the Effect of Mutual Coupling in Ultra-Wideband-Multi-Band Multiple Input Multiple Output Systems

Rocco Vincent Dragone Jr.
Advisor: Kapil R. Dandekar, Ph.D.

The combination of ultra-wideband (UWB) spectrum with Multiple-Input Multiple-Output (MIMO) system techniques show great promise for developing very high bandwidth wireless personal area networks (WPANs). While these networks have been explored in theory, there is little literature regarding the practical limitations of this technology. Specifically, the mutual coupling between the antennas in the system is usually ignored.

This thesis quantifies the effects of mutual coupling in MIMO UWB systems. A variety of antenna geometries and spacings were simulated. Several scenarios in a typical WPAN environment were simulated using electromagnetic ray tracing (ERT) techniques. These results were validated using network analyzer channel measurements. These results show mutual coupling has a significant impact on channel capacity. Furthermore, in most scenarios, mutual coupling can actually improve the channel capacity by decorrelating adjacent spatial channels. Knowledge of this potential benefit of mutual coupling in MIMO-UWB systems will allow future WPAN designers to develop systems using small, multi-antenna devices with very high capacities.

1. Introduction

1.1 Motivation

The concept of ultra-wideband (UWB) radio was first developed several decades ago, however only recently has the area garnered a large research interest in the field of wireless communications. This recent interest is due to two developments. First, hardware is now available that operates at the speeds required for successful, high-capacity UWB communication. Secondly, in 2002, the FCC updated their regulations regarding ultra-wideband radio systems. The FCC defines an UWB signal as a signals whose bandwidth is greater than 1.25 GHz or whose fractional bandwidth is greater than 0.25. UWB communication systems have been allocated the frequency band of 3.1 to 10.6 GHz (Figure 1.1). The maximum signal power is limited to -41.3 dBm per MHz [12]. This newly opened bandwidth will allow the development of very high capacity, short range networks with data rates up to and possibly exceeding 528 Mbps [10].

Since Foschini's pioneering work [14], mulitple-input mulitple-output (MIMO) systems have been shown to have significant capacity gains over single-input single-output (SISO) systems in a variety of situations. Much research leveraging MIMO techniques in UWB systems has already been performed [20] [38] [33]. However, there is a lack of literature exploring the effects of mutual coupling in these systems. In non-UWB systems, mutual coupling has been shown to have a significant impact on channel capacity [6] [35] [26]. The effect of mutual coupling is based on the spatial correlation of adjacent channels in a system, the antenna geometry, and the separation of the antenna elements. A comprehensive study of these factors has yet to be performed. This thesis aims to fill this gap in the research through a combina-
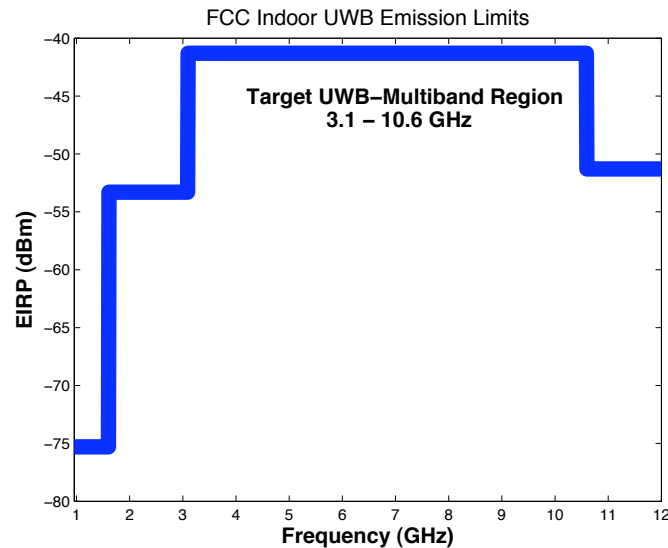
Figure 1.1: FCC Regulations on UWB

tion of antenna and channel simulation and field measurements using custom channel sounding equipment.

1.2 Related Work

1.2.1 UWB Antenna Design

With the rising popularity of UWB systems, there has been a surge in UWB antenna designs. Old frequency independent designs have been revisited [9] [34] while new and innovating antenna designs have been proposed [37] [30] [33]. UWB antenna design poses a number of problems. Antennas must be kept small in order to be useful in UWB applications, such as wireless USB transmission, while at the same time maintaining a very wide bandwidth. The antenna must be impedance matched over the entire UWB spectrum in order to minimize return losses in the system. This is especially important in UWB systems as the transmit power is already very low. Additionally, it is desirable for the antenna to maintain the same radiation pattern over the UWB bandwidth so that all the assigned frequency bands can be exploited.

1.2.2 Mutual Coupling in MIMO Systems

The desired use for UWB systems is in wireless personal area networks (WPAN). This application involving compact form factor devices implies small overall system design. If antennas are to be used in the system, they must be placed very near to each other. The close proximity of these antennas causes mutual coupling. The effects of mutual coupling in narrowband systems are varied [6]. In non-line of sight (NLOS) environments, mutual coupling increases the correlation between spatial channels causing a decrease in capacity [13]. However, in line of sight (LOS) environments mutual coupling can decorrelate adjacent channels [35]. These environments can also be classified as those with rich scattering environments (NLOS) and those with poor scattering environments (LOS) [6]. The target WPAN environment will likely be rich with scatterers. This leads to the hypothesis that mutual coupling will decrease performance. However, at the time of this writing, a comprehensive study on mutual coupling in UWB systems does not exist.

1.2.3 UWB MIMO Channel models

While several statistical models for UWB propagation are available [22] [23] [5], none take into account the mutual coupling between antennas. Several cluster models have been proposed for modeling the multipath components in an UWB system including both Nakagami and Poisson distrubutions. The parameters for these models are highly dependent on the environment being simulated. The literature is primarily concerned with the wireless channel between antennas often making simplifying assumptions about the antennas themselves. This leads to ideal channel models that do not accurately reflect the entire system.

1.3   Contributions

This thesis will explore and quantify the effects of mutual coupling in UWB-MB MIMO systems. Computational electromagnetics will be used to simulate the effect of mutual coupling over the entire UWB frequency range. Channel measurements will be taken in the presence of mutual coupling to validate these simulations. This is different from typical UWB-MIMO channel measurements where 'synthetic' arrays are used.

1.4   Thesis Organization

Chapter 2 of this thesis provides a background introduction to topics which will be discussed throughout this document, including mutual coupling, channel capacity, and MIMO communication. Chapter 3 discusses the design, fabrication, and measurements of several antennas. Chapter 4 discusses electromagnetic ray tracing. Chapter 5 presents experimental validation for the ERT results. Chapter 6 concludes this thesis by providing a brief summary of this thesis as well as motivating future work.

1.5   Table of Symbols

This section includes a table of symbols in order of their appearance.

Table 1.1: Table of Symbols

Symbol	Definition	Size (if non-scalar)
λ	Wavelength	
y(t,τ)	Received Signal (continuous time domain)	
s(t,τ)	Sent Signal (continuous time domain)	
h(t,τ)	Channel Impulse Response (continuous time domain)	
$y_(n)$	Received Signal (discrete time domain)	
$s_(n)$	Sent Signal (discrete time domain)	
$h_(n)$	Channel Impulse Response Signal (discrete time domain)	
Y(k)	Received Signal (Frequency Domain)	
S(k)	Sent Signal(Frequency Domain)	
H(k)	Channel Frequency Response (Frequency Domain)	
M_t	Number of transmitting antennas	
M_r	Number of receiving antennas	
$\overrightarrow{y}_n$	Vector of Received Signals	M_rx1
$\overrightarrow{s}_n$	Vector of Sent Signals	1xM_t
$\widetilde{\mathbf{H}}(k)$	MIMO Channel Frequency Response	M_txM_r
C_t	Mutual Coupling Matrix of Transmitter	M_txM_t
C_r	Mutual Coupling Matrix of Receiver	M_rxM_r
$\widetilde{\mathbf{H}}(k)_{C,band}$	$\widetilde{\mathbf{H}}(k)$ with mutual coupling *band*	M_txM_r
$\widetilde{\mathbf{H}}(k)_{NoC,band}$	$\widetilde{\mathbf{H}}(k)$ without mutual coupling at frequency band *band*	M_txM_r
r_x	x-radius length for single-ended elliptical antenna	
r_y	y-radius length for single-ended elliptical antenna	
r_1	Spiral Radius	
E_ϕ	Electric Field in Phi direction	
E_θ	Electric Field in Theta direction	
G_ϕ	Antenna Gain in Phi direction	
G_θ	Antenna Gain in Theta direction	
η	Normalization Factor	
N	Number of frequency bands (14)	

2. Background

This chapter will provided introductions to several of the topics necessary for understanding the remainder of the thesis. Section 2.1 discusses multi-band UWB. In Section 2.2 the MIMO-UWB channel model is developed. Section 2.3 will discusses the computational electromagnetic simulations performed in this thesis and Section 2.4 describes the metrics used to quantify performance.

2.1 Multi-band UWB

Ultra wideband (UWB) systems have attracted much interest in recent research [11] [22] [36]. There is great potential for increasing the spectral and spatial efficiency of UWB systems by applying multiple-input multiple-output (MIMO) techniques, which take advantage of channel spatial characteristics. The current European Computer Manufacturers Association (ECMA) standard for multi-band UWB is given in [10]. Multi-band means that UWB spectrum into several frequency bands which are 528 MHz wide. UWB systems are to use frequency hopping, a spread spectrum technique which increases the signals resistance to narrowband interference. Frequency hopping will be performed pseudorandomly between each of the assigned bands. These bands are shown in Table 2.1. Analysis of the antenna effects and far field propagation in each of these frequency bands will be performed. This will be done by simulating for both the channel and the antenna at the center frequency of each band as shown in Table 2.1.

Band	1	2	3	4	5	6	7
f_c (GHz)	3.432	3.960	4.488	5.016	5.544	6.072	6.600
Band	8	9	10	11	12	13	14
f_c (GHz)	7.128	7.656	8.184	8.712	9.240	9.768	10.296

Table 2.1: ECMA UWB Frequency Bands

2.2 MIMO-UWB Channel Model

2.2.1 SISO Channel Model

The first step in developing a MIMO-UWB channel model is to examine the narrowband single-input single-output (SISO) case for a single transmitting/receiving antenna pair. The signal experiences multipath fading as a function of the geometry of the indoor environment. Assuming a linearly (vertically) polarized antenna for simplicity, the channel impulse response is given as in [18]:

$$h(t, \tau) = \sum_{i=0}^{N-1} E_z^{(i)}(t)\delta(t - \tau_i) \tag{2.1}$$

where N is the total number of multipath components, $E_z^{(i)}$ is the complex amplitude of the ith multipath component, and τ_i is the delay associated with that multipath component.

The channel input-output response can be written as:

$$y(t, \tau) = h(t, \tau) * s(t, \tau) \tag{2.2}$$

where $y(t, \tau)$ is the received signal, $s(t, \tau)$ is the sent signal, and $h(t, \tau)$ is from Equation 2.1.

Electromagnetic ray tracing methods have the potential to calculate multipath components whose time of arrivals are very similar [8]. A realistic finite bandwidth

receiver will only be able to resolve these multipath components to a certain degree. In the interest of later verifying these simulations with experimental data, we organize the multipath components into resolvable clusters. A cluster size of 2 ns for an UWB indoor channels is suggested in [5]. The channel impulse response, sent signal, and received signal can be discretized using this cluster size.

$$\mathbf{y} = (y_0, ..., y_{N-1}) \tag{2.3}$$

$$\mathbf{s} = (s_0, ..., s_{N-1}) \tag{2.4}$$

$$\mathbf{h} = (h_0, ..., h_{N-1}) \tag{2.5}$$

where N is the total number of bins. Using this notation, the received signal can be written as

$$\mathbf{y}_n = \sum_{l=0}^{N-1} h_l s_{n-l} \tag{2.6}$$

Taking the discrete Fourier transform of Equation 2.6, we get:

$$Y(k) = H(k)S(k) \tag{2.7}$$

where Y(k) is the discrete Fourier transform of $y(t, \tau)$, S(k) is the discrete Fourier transform of $s(t, \tau)$, and H(k) is the discrete Fourier transform of $h(t, \tau)$. Note that the convolution is now a multiplication.

2.2.2   MIMO Channel Model

We next define the input output relationship of a MIMO channel with M_r receiving antennas and M_t transmitting antennas as in [4]

$$\overrightarrow{Y}(k) = \widetilde{\mathbf{H}}(\mathbf{k})\,\overrightarrow{S}(k) \tag{2.8}$$

where $\overrightarrow{Y}(\mathbf{k})$ is a vector of length M_r of received signals, $\overrightarrow{S}(\mathbf{k})$ is a vector of length M_t of transmitted signals, and $\widetilde{\mathbf{H}}(k)$ is a M_r x M_t complex-valued matrix with each entry $\widetilde{\mathbf{H}}_{\mathbf{m,n}}(k)$ representing the SISO link between the nth transmit antenna and the mth receiver. For example, in a system with two transmitting and receiving antennas:

$$\widetilde{\mathbf{H}}(\mathbf{k}) = \begin{bmatrix} H_{11}(k) & H_{12}(k) \\ H_{21}(k) & H_{22}(k) \end{bmatrix} \tag{2.9}$$

where $H_{m,n}(k)$ is derived from Equation 2.7 using the path between the mth transmitting antenna and nth receiving antenna.

2.2.3   Mutual Coupling

Mutual coupling occurs when antennas are placed within close proximity to each other. The field generated by one antenna affects the current distribution in nearby elements [17]. Accounting for mutual coupling can be done by modifying our channel model as in Equation 2.10 [6].

$$\overrightarrow{Y} = \mathbf{C}_r \widetilde{\mathbf{H}} \mathbf{C}_{\mathbf{t}}\,\overrightarrow{S} \tag{2.10}$$

where $\mathbf{C}_r$ denotes the coupling matrix at the receiver and $\mathbf{C}_t$ denotes the coupling matrix at the transmitter. Letting

$$\widetilde{\mathbf{H}}_{\mathbf{C}} = \mathbf{C}_r \widetilde{\mathbf{H}} \mathbf{C}_t \tag{2.11}$$

we can rewrite Equation 2.10 as

$$\overrightarrow{Y} = \widetilde{\mathbf{H}}_{\mathbf{C}} \overrightarrow{S} \tag{2.12}$$

The coupling matrix for a narrowband dipole antennas is defined in Equation 2.13 from [15].

$$\mathbf{C} = \begin{bmatrix} a & b \\ b & a \end{bmatrix} (Z_T + Z_A)(\mathbf{Z} + Z_T\mathbf{I})^{-1} \tag{2.13}$$

where Z_T is the load impedance of each element, Z_A is the antenna impedance, $\mathbf{Z}$ is the mutual impedance matrix, and $\mathbf{I}$ is the identity matrix . This coupling causes a change in the radiation pattern which can be expressed as in Equation 2.14 [6]. For the case of two antennas located at the same elevation, separated by a distance d in the azimuthal plane, the coupling transforms the radiation pattern as:

$$g_d(\phi) = g_s(\phi) \left(a + b e^{j2\pi \frac{d}{\lambda} \cos \phi} \right) \tag{2.14}$$

where $g_d(\phi)$ is the radiation pattern of an antenna with an adjacent element at a distance d, and $g_s(\phi)$ is the radiation pattern of a single antenna with no mutual

coupling considered. Note that the change is radiation pattern is dependent on the distance separating the two elements. The variables a and b are from the coupling matrix in Equation 2.13.

Evaluating $\mathbf{C}$ (and therefore $g_d(\phi)$) for non-dipole antennas is non-trivial [6]. Alternate antenna geometries invalidate several of the assumptions made in the derivation of $\mathbf{C}$ in [17]. Rather than attempting to derive a new, mathematically complex form of the coupling matrix for each antenna geometry, this thesis will evaluate the radiation patterns of antennas in the presence of mutual coupling by using electromagnetic simulation. These patterns will then be applied to the results from the electromagnetic ray tracer, discussed in detail in Section 2.3, thus forming $\mathbf{H_c}$ directly from computational electromagnetic simulation results.

2.2.4 Multi-band UWB MIMO Channel Model

The model in 2.15 will be extended to multi-band UWB by simply denoting a different channel response for each frequency band.

$$\overrightarrow{Y}(k) = \widetilde{\mathbf{H}}_{\mathbf{C,band}} \overrightarrow{S}(k) \tag{2.15}$$

where *band* denotes which frequency band is being considered (1 through 14). It will be shown in Chapter 4 that there is a significant difference between the various $\mathbf{H}_{bands}$.

2.2.5 Statistical Channel Model

The UWB MIMO channel has not been studied extensively in the literature, however a modified Kronecker model has been proposed [19]. The Kronecker model assumes the channel correlation at the transmit and receive antennas are independent.

The channel model is given as:

$$\widehat{\mathbf{H}} = \mathbf{R}_{RX}^{\frac{1}{2}}\mathbf{G}(\mathbf{R}_{TX}^{\frac{1}{2}}))^T \tag{2.16}$$

where $\mathbf{H}$ is the channel matrix, $\mathbf{R}_{RX}$ is the receiver correlation matrix, $\mathbf{R}_{TX}$ is the receiver correlation matrix, and $\mathbf{G}$ is a random matrix whose elements are randomly determined based on environmental characteristics. This differs from the typical Kronecker model [27], in which $\mathbf{G}$ is created from a Gaussian distribution. This model does not include mutual coupling as $\mathbf{R}_{RX}$ and $\mathbf{R}_{TX}$ do not account for mutual coupling of the antennas.

2.3   Computational Electromagnetic Simulation

This thesis will use two types of computational electromagnetic simulation (CES). The MIMO channel ($\widetilde{\mathbf{H}}_{\mathbf{C}}$ from Equation 2.15)will be simulated using FASANT [28], an electromagnetic ray tracer (ERT). More details regarding the ERT will be included in Chapter 4. The antenna effects will be simulated using HFSS [3] which utilizes a 3D full-wave finite element method to compute the electrical behavior of high-frequency and high-speed components [3]. Mutual coupling is considered by exciting only one element at a time while each of the other elements is terminated with an 50 Ω (matched) load.

CES has been used extensively in literature before to simulate the narrowband channel [16] [29] [18]. However, to accurately simulate MIMO-UWB multiband systems, some issues must be considered. The antenna patterns are not flat over the entire UWB spectrum as will be shown in Chapter 3, so analysis of the mutual coupling needs to be considered at the center frequency of each band. Additionally, as the channel is frequency selective, the impulse response of the channel is not the same

over the UWB spectrum (as will be shown in Chapter 4), so we must also simulate the channel at the center frequency of each of the bands.

$\widetilde{\mathbf{H}}_{\mathbf{C}}$ is calculated by combining the results from FASANT with the results from HFSS. FASANT takes a radiation pattern (from HFSS) as one of its input and applies it to the transmitting signal. The output of FASANT is each multipath component impinging from a transmitting antenna to a receiving location. The angle of arrival and electric field of each component is given. Radiation patterns are specified in terms of gain at arrival angle. The suitable gain from the radiation pattern is applied to the multipath component. Summing these electric field elements as in Equation 2.1 is performed. This process is done for each transmitter antenna pair to form $\mathbf{H}_c$. These simulations are performed at the center frequency of each of the UWB frequency bands, forming 14 different $\widetilde{\mathbf{H}}_{\mathbf{C,band}}$ for each link examined.

The HFSS simulations will be verified in an anechoic chamber. The whole system will be verified using the channel sounding experiment described in Chapter 5.

2.4 Performance Evaluation

This section will describe the methods used to quantify the effects of mutual coupling in the MIMO-UWB system. The spatial correlation between adjacent channels with and without mutual coupling will be derived. Additionally, channel capacity using several different transmitting schemes will be examined.

2.4.1 Spatial Correlation

If multiple antennas are used, the channel between different spatially separated transmitting and receiving antennas will be of different quality. This is known as spatial diversity. UWB signals exhibit high spatial diversity due to the very high number of multipath components present in a typical environment [5]. Therefore,
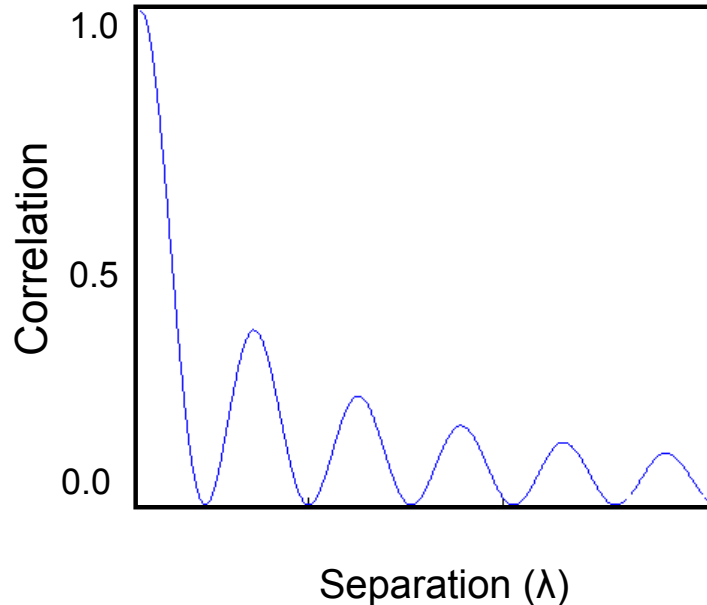
Figure 2.1: Simple case illustrating spatial correlation

small variations in location (distance between antennas in the receiving/transmitting array) can lead to vastly different channels. It is a standard assumption that waves are incident from all angles at the receiver, thus points of positive and negative interference of multipath components are spaced approximately $\frac{\lambda}{2}$ apart due to their sinusoidal nature. In a simple scenario, where two waves are impinging on an array of antennas, the correlation of the signal at each receiver takes the shape as a Bessel function [21] as shown in Figure 2.1. This is a simple scenario, assuming only two impinging waves. However, it provides insight into the relationship between antenna spacing and spatial correlation.

This thesis examines a realistic MIMO-UWB system where the distance between antennas is fixed, but the full UWB frequency spectrum is used. Since frequency hopping is used, λ is not a constant in the system. Therefore, no single distance can assure decorrelated channels at all frequencies. It is necessary to define the

correlation between adjacent channels without any reference to wavelength. The spatial correlation between antennas l and m is given as in [29]:

$$r_{l,m} = \frac{\int_{4\pi} \sqrt{P_l(\Omega)} G_l(\Omega) G_m(\Omega)^* \sqrt{P_m(\Omega)}\, d\Omega}{\sqrt{\int_{4\pi} P_l(\Omega)|G_l(\Omega)|^2 d\Omega}\sqrt{\int_{4\pi} P_m(\Omega)|G_m(\Omega)|^2 d\Omega}} \tag{2.17}$$

where Ω encompasses both the elevation and azimuth angles, $P(\Omega)$ is the power angular spectrum of the received signal and $G_l(\Omega)$ denotes the far-field radiation pattern of the lth antenna.

2.4.2 Capacity

Equal Power Allocation

An open loop system is one where the transmitter has no knowledge of the channel In this case, power is allocated uniformly across all subchannels. The capacity at a given frequency band is [14]

$$C_{eq,band} = log_2\Big(det(I_{M_r} + \frac{SNR}{M_t}\widetilde{\mathbf{H}}_{C,band}\widetilde{\mathbf{H}}_{C,band}^H)\Big) \tag{2.18}$$

where, SNR is the received signal to noise ratio, M_r and M_t are the number of receiving and transmitting antennas respectively, $det(\mathbf{X})$ denotes the determinant of matrix $\mathbf{X}$, and $\mathbf{H}^H$ denotes the complex conjugate transpose of matrix $\mathbf{H}$. This metric is useful as it represents the capacity of the MIMO-UWB channel with no feedback from the receiver required.

Waterfilling

Before examining closed loop capacity systems, a singular value decomposition is performed on $\widetilde{\mathbf{H}}_{C,band}$ as follows:

$$\widetilde{\mathbf{H}}_{C,band} = \mathbf{U}\mathbf{\Sigma}\mathbf{W}^H \tag{2.19}$$

where the singular values forming the matrix $\mathbf{\Sigma}$ represent the eigenmodes of the system

$$\mathbf{\Sigma} = \begin{bmatrix} \sigma_1 & 0 \\ 0 & \sigma_2 \end{bmatrix} \tag{2.20}$$

and $\mathbf{U}$ and $\mathbf{W}$ contain the beamforming and recombining vectors associated with each eigenmode.

A closed loop system is one where the transmitter has knowledge of the channel and is able to use it with no delay. This allows the transmitter to take advantage of the differences in the channels. In waterfilling, the transmitter spends most of the transmitter power on those links with high SNRs. The transmitter uses less power on those channels with lower SNRs [21]. If there is not enough power available, the transmitter will not use poor channels at all. In a closed loop system, the optimal capacity is given by the waterfilling distribution [7]:

$$C_{wf,band} = \sum_{i=1}^{M_t} log_2\Big(1 + \sigma_i^2(\mu - \frac{1}{\sigma_i^2})^+\Big) \tag{2.21}$$

where μ is the "water-level", σ_i is the ith singular value of the $\widetilde{\mathbf{H}}_{C,band}$ matrix, and $(\bullet)^+$ indicates $\max(0, \bullet)$. The "water-level" is calculated numerically via:

$$SNR = \sum_{i=1}^{M_r} \left(\mu - \frac{1}{\sigma_i^2} \right)^+ \qquad (2.22)$$

where σ_i is the ith singular value of the $\widetilde{\mathbf{H}}_{C,band}$ matrix from equation 2.18, and $(\bullet)^+ = max(0, \bullet)$. This calculation is useful as it will take advantage of the different available eigenmodes. However, it requires significant overhead for the receiver to relay channel information to the transmitter. Additionally, the transmitter must do some signal processing to compute the best waterfilling distribution.

Beamforming

Another closed loop method for increasing performance is beamforming. Beamforming takes advantage of knowledge of the channel by changing the directionality of the beam to avoid interference. It directs all the transmitter power into the strongest eigenmode. The capacity using in beamforming [24] is given as:

$$C_{beam,band} = log_2 \left(1 + SNR\sigma_{max}^2 \right) \qquad (2.23)$$

where σ_{max} is the maximum singular value of the SVD decomposition of the channel matrix $\widetilde{\mathbf{H}}_{C,band}$. This metric is useful as it gives a much higher capacity than equal power allocation. However, it requires less computation on the part of transmitter than waterfilling.

3. Antenna Design and Measurement

UWB antenna design offers a variety of challenges. Not only are broadband (3.1-10.6 GHz) impedance matching characteristics a prerequisite, but it is highly desirable for the antenna to be small for use in WPAN devices. Additionally, an omnidirectional pattern is desirable so that devices in the WPAN do not have to maintain a specific orientation. In this chapter, we will examine three antenna geometries: one commercially available antenna and two that were fabricated for this project. These custom geometries were chosen because literature showed them to have very wideband impedance matching as well as radiation patterns omnidirectional in the azimuthal plane [9][30][31]. These antennas will be analyzed and evaluated based on their voltage standing wave ratio (VSWR), radiation patterns, and physical size. The VSWR is an indication of how much power is being reflected back at the antenna feed port and a value of less than 2 corresponds to less than a 10% power loss [32]. A value higher than 2 indicates a significant power loss. After the antennas were fabricated, they were measured in Drexel University's anechoic chamber (TDK Corporation). An anechoic chamber is a shielded room designed to stop all electromagnetic interference. It allows for highly accurate antenna measurements.

3.1 Commercially Available Antennas

There are few commercially available antennas for UWB systems. Drexel Wireless Systems Lab has purchased several patch antennas from Fractus [2] (seen in Figure 3.1). The antennas are small patch antennas whose dimensions are 10x10x0.8 mm. However, the antennas need to be mounted on a board where a microstrip impedance matches the antenna to the feed. The total dimensions of this antenna are 3.5x2

centimeters. While these antennas have an ultra slim profile, they are only useful for the 3-7GHz range. The measured VSWR is shown in Figure 3.2 where the "cutoff" line indicates a VSWR of 2. It is highly desirable that the VSWR is below this line for all frequencies used. The measured values closely match those advertised in [2]. This antenna is suitable for the frequency bands below 7 GHz (Bands 1-7). Above 7 GHz, a significant amount of power is lost in feeding the antenna. The measured radiation pattern of the Fractus antenna is shown in Figure 3.3.
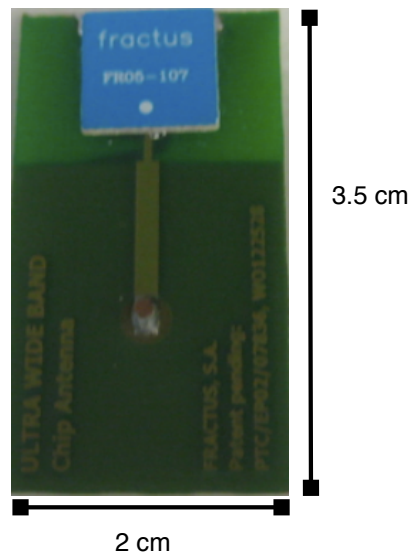
Figure 3.1: Fractus Patch Antenna

3.2 Spiral Antenna

An early pioneer in the study of frequency-independent antennas was Victor H. Rumsey. He first proposed the principle that the impedance and pattern properties of an antenna will be frequency independent if the antenna shape is specified only in
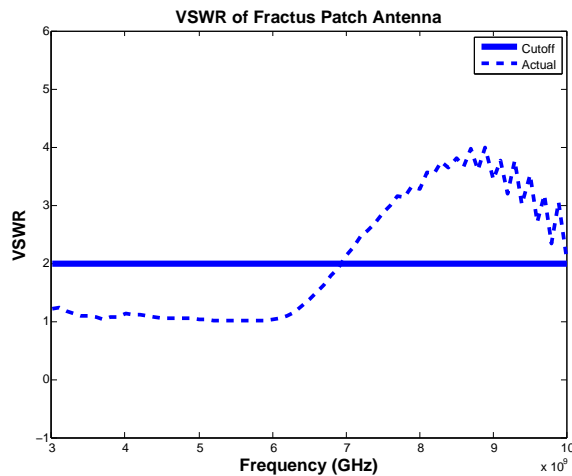
Figure 3.2: Measured VSWR of Fractus Patch Antenna

terms of angle [34]. His work was later experimentally verified by Dyson in [9].

A logarithmic spiral is defined by Equation 3.1 [17]:

$$r_1 = a^\theta \tag{3.1}$$

where r_1 is the radial distance to a point at the angle of θ to the x-axis and a is a constant. From this equation, it is obvious that the logarithmic spiral is dependent only on θ and therefore meets the requirements in Rumsey's principle for frequency independent antennas.
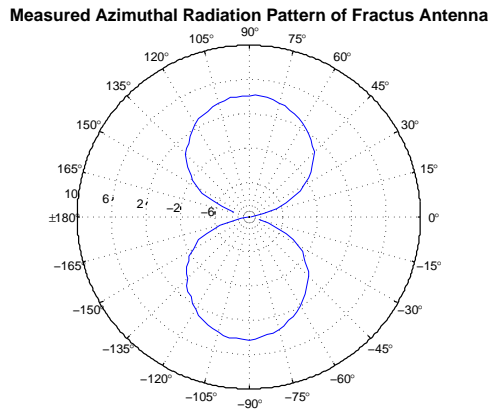
Figure 3.3: Azimuthal Radiation Pattern of Fractus Antenna at 3.492 GHz

3.2.1 Design of Spiral Antenna

To create a logarithmic spiral antenna, one needs only to create a spiral, create a rotated version of the spiral (Equation 3.2), and then metallize the surface in between.

$$r_2 = a^{\theta - \frac{\pi}{2}} \tag{3.2}$$

Additionally, according to Mushiake [25], in order for an antenna to have a constant impedance an antenna must be self-complementary in shape. To meet this requirement, we must duplicate the spiral arm and shift by an angular rotation of 180°. Following these steps and choosing a to be 1.247 we generate the geometry in Figure 3.4.
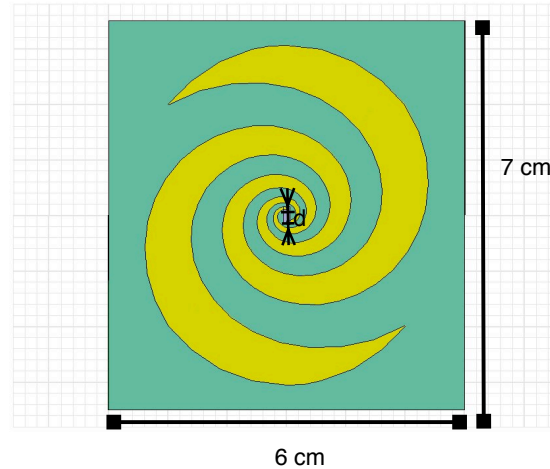
Figure 3.4: Design of Spiral Antenna

3.2.2 Simulation of Spiral Antenna

The primary concern when optimizing the antenna was to achieve wideband impedance matching. To this end, several spiral arm lengths were simulated. Additionally, different substrates were simulated. The best results are seen with very thick substrates (1.5 centimeters), with high dielectric constant (10). However, in the interest of building an antenna with a slim profile, and using materials readily available, an FR4 substrate of thickness 59 mils was chosen. Also, increasing the spiral arm length increased bandwidth of the antenna. However, considering the design objective of a reasonable small antenna, we limit the total antenna dimensions to 7 cm by 6 cm. The final geometry is shown in Figure 3.4. The distance between the spiral arms, d, is minimized but large enough to allow feeds. This distance determines the highest frequency the antenna should be impedance matched for. Simulations showed that tapering the ends of the spiral arms allowed for wider band impedance matching. The

simulated and measured VSWR of the antenna is shown in Figure 3.5. The simulated antenna shows a VSWR of less than 2 for most of the 3-11 GHz bandwidth. The azimuthal radiation pattern of a single antenna is shown in Figure 3.6.
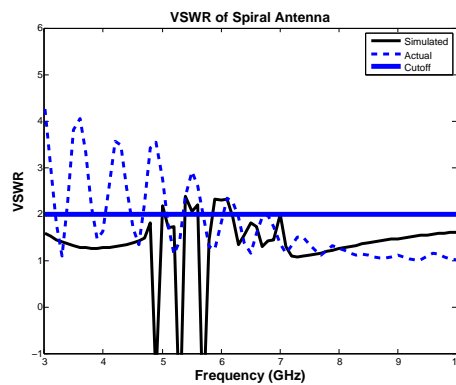

Figure 3.5: VSWR of Spiral Antenna

3.2.3 Fabrication of Spiral Antenna

The antenna was fabricated using DWSL's milling machine (T-Tech-QC5000) on 59 mil FR4. The antenna is fed by attaching an SMA-connector to one spiral arm and grounding the other. The actual and simulated VSWR are shown in Figure 3.5. The fabricated antenna is shown in Figure 3.7. The fabricated antenna did not perform as well as in simulation, probably due to the finite thickness of the spiral arms. For undetermined reasons, the antenna did not behave as expected at low frequencies. The measured VSWR is significantly larger than 2 at frequencies less

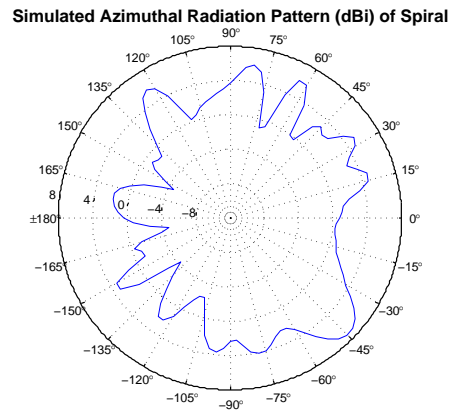**Simulated Azimuthal Radiation Pattern (dBi) of Spiral**

Figure 3.6: Spiral Azimuthal Radiation Pattern at 7.128 GHz

than 6 GHz. This means that the antenna is unusable for the frequency bands in the 3-6 GHz range. As mentioned above, lengthening the spiral arms should improve the low frequency response, however this would conflict with the size restraints.

3.3 Single Ended Elliptical Antenna

The single ended elliptical antenna (SEA) design [31] takes the well known circular disc monopole antenna [30] and compresses it down to a single plane. The main advantages to this antenna are an ultra slim profile and large bandwidth. Since the ground is coplanar with the antenna, the thickness of the antenna is very slim.

3.3.1 Design of SEA

The design for the SEA is adapted from the design in [31]. The equation for defining the lowest operating frequency is:

Figure 3.7: Fabricated Spiral

$$f = \frac{30(2.4)}{L + r} GHz \tag{3.3}$$

where L=2*r_y in cm and r=$\frac{r_x}{4}$ in cm. These values are shown in Figure 3.8. One possible solution for a lower bound of 3.168 GHz is an ellipse with a y-radius of 1.03 cm and x-radius of 0.91 cm. With the coplanar ground plane, the dimensions of the antenna is 3.81x2.67 centimeters with a thickness of 7 mils. The optimal size of the ground plane component was determined via simulation. The presented design is the smallest simulated design that maintained the required impedance matching over the whole UWB spectrum of 3-11 GHz.
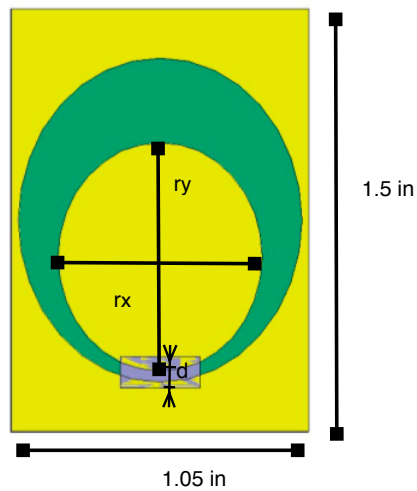
Figure 3.8: Design of SEA Antenna

3.3.2 Simulation of SEA

The distance from the radiating ellipse to the ground feed (d in Figure 3.8) is one of the most important parameters for the performance of the SEA. Moving the radiating ellipse closer to the feed lowered the maximum frequency while increasing the lower frequency bound. A parametric analysis was performed to determine which spacing best impedance matched for the UWB frequency range (3-11 GHz). The distance was swept from 10 - 60 mils in steps of 5 mils with the VSWR being measured at all steps. Aa distance of 40 mils gave the best performance. The simulated azimuthal radiation pattern of a single antenna is shown in Figure3.10 .
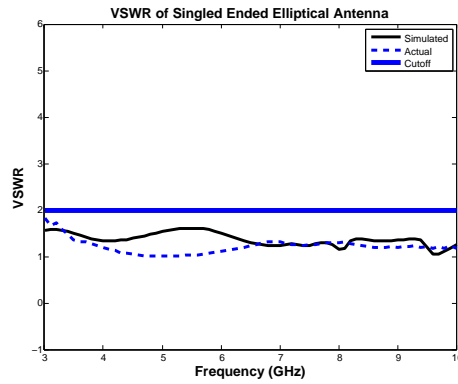
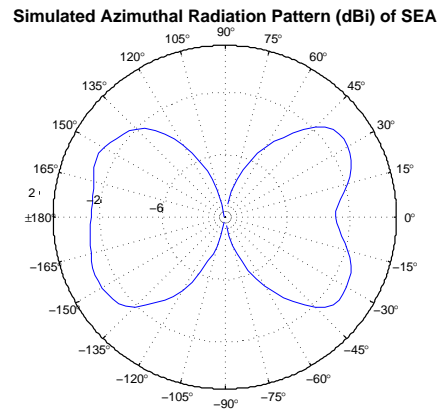Figure 3.9: VSWR of Single Ended Elliptical Antenna

Figure 3.10: SEA Simulated Azimuthal Radiation Pattern

3.3.3 Fabrication of SEA

The antenna was fabricated using DWSL's milling machine (T-Tech -QC5000) on the thinnest substrate available: 7 mil FR4. The antenna is fed by attaching an

SMA-connector to the radiating center ellipse and grounding it onto the coplanar ground. The actual and simulated VSWR are shown in Figure 3.9. The fabricated antenna is shown in Figure 3.11. The fabricated antenna slightly outperforms the simulated one.
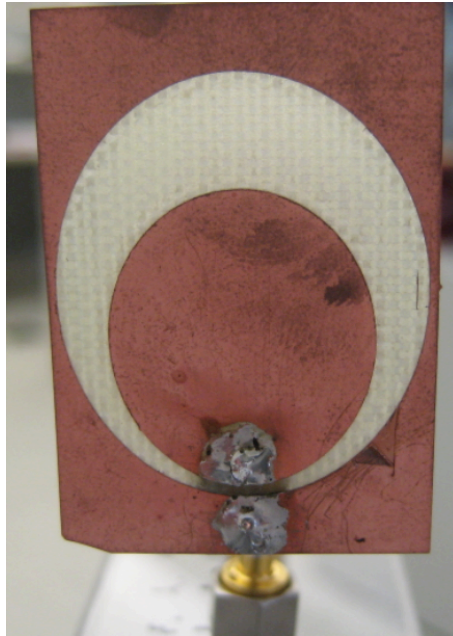
Figure 3.11: Fabricated SEA

3.4   Comparison

The single-ended elliptical antenna outperformed both the commercially available Fractus antenna and spiral antenna in terms of bandwidth with acceptable return loss. All the antennas had near-omnidirectional radiation patterns. While the SEA is slightly larger in physical dimensions than the Fractus antenna, it is by far the better performer. The small increase in size allows solid performance over 10 additional

Antenna	Size	Bandwidth	Radiation Pattern in azimuthal plane
Fractus	3.5x2 cm	3-7 GHz	Omnidirectional with noticeable dip
SEA	3.81x2.67 cm	3-11 GHz	Smoothly Omnidirectional
Sprial	7x6 cm	6.5-11 GHz	Roughly Omnidirectional

Table 3.1: Antenna Comparison

UWB frequency bands. For comparison, the radiation patterns of the Spiral antenna, SEA, and Fractus antenna are compared in Figure 3.12. They are displayed on a Cartesian plot for clarity. The spiral antenna has the highest overall gain, however the radiation pattern is not smooth. The SEA antenna has lower gain on average than either antenna, however it also shows the least variance. Table 3.1 summarizes these observations.
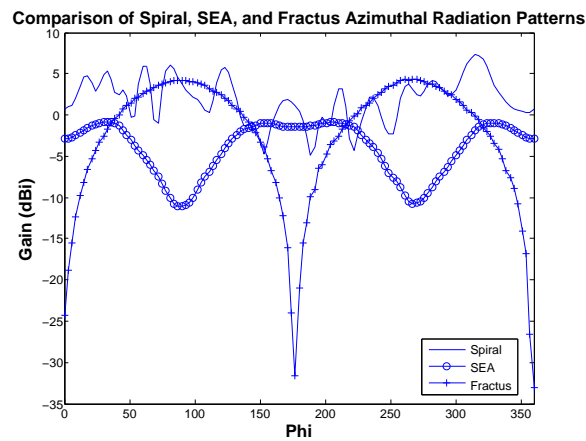

Figure 3.12: Comparison of Spiral and SEA Radiation Patterns

3.5 Antenna Array

Based on this analysis, the SEA is clearly the best choice due to its extremely broad impedance matching and small size. Therefore, the remainder of this thesis will use the SEA. A comparison of the radiation pattern of the fabricated antenna to the simulated one is shown in Figure 3.13. The fabricated radiation pattern has slightly less gain than the simulated antenna. Additionally, the radiation pattern is less smooth. However, the measured radiation pattern maintains the same general shape as the simulated results and can still be considered roughly omnidirectional.
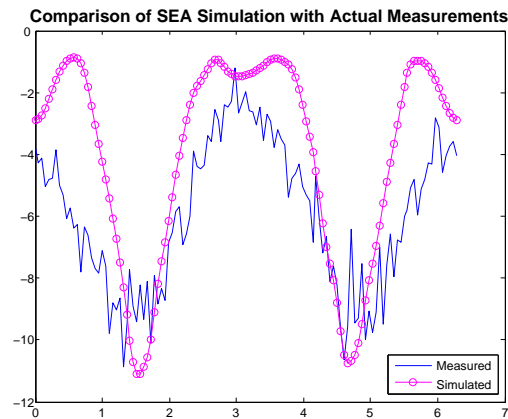
Figure 3.13: Comparison of measured and simulated SEA patterns

It is also important to note the effect that mutual coupling (MC) has on the radiation patterns. As can be seen from the radiation patterns, moving an adjacent antenna element closer to the transmitting antenna disturbs the radiation pattern. These changes effect the spatial correlation between adjacent channels in the MIMO UWB system as will be discussed in Chapter 4. The simulated effects of mutual coupling are shown in Figure 3.14. The measured effects of mutual coupling are

shown in Figure 3.15. The results displayed are with a terminated antenna element placed $\frac{\lambda}{2}$ from the radiating antenna element The λ being considered is the wavelength related to the lowest frequency band, 3.492 GHz. This corresponds to a value of 4.37 centimeters.
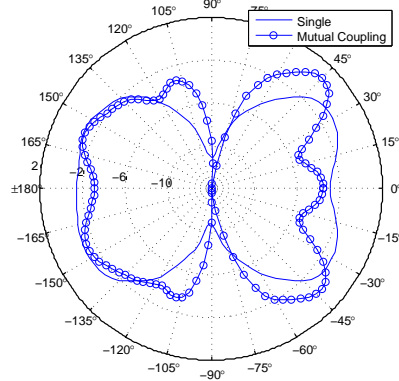
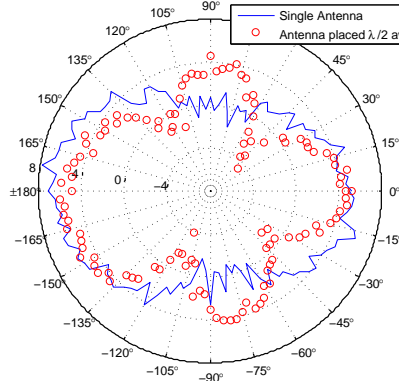Figure 3.14: Comparison of SEA Simulated Radiation Patterns with and without MC

Figure 3.15: Comparison of SEA Measured Radiation Patterns with and without MC

4. Simulations

4.1   FASANT Simulations

The FASANT simulation system [1] uses electromagnetic ray tracing to compute the received signal at a given distance from a given transmitter. It works by computing each ray component from the transmitter to receiver. The calculations performed by FASANT are based on the Geometric Theory of Diffraction in its uniform version [28]. The simulations performed for this thesis calculate the rays received due to the following propagation mechanisms: direct, reflected, diffracted, double reflected, reflected-diffracted, diffracted-reflected and diffracted-diffracted. The FASANT simulation accepts a transmitter antenna radiation pattern as an input. The link from each transmitting antenna to each receiving antenna is simulated individually, using the simulated radiation patterns discussed in Chapter 3. The output of FASANT gives the complex magnitude of each ray arriving at a particular receiver along with the path length that the ray traveled. FASANT also generates data that describes all of the intermediate points a ray travels to between the transmitter and the receiver. Using this information, it is possible to find the angle of arrival of each ray, or multipath component, at the receiver. FASANT provides the electric field components in the x, y, and z-directions. With knowledge of the angle of arrival, this can be converted into electric field components in the θ and ϕ directions. These field components were then multiplied by the appropriate field component from the antenna radiation pattern as in Equations 4.1 and 4.2 to find the actual received electric field for that ray.

$$E_\theta^{(i)}(\theta, \phi) = E_{\theta, ERT}^{(i)}(\theta, \phi) A_\theta(\theta, \phi) \tag{4.1}$$

where $A_\theta(\theta, \phi)$ is the far field radiation pattern of the antenna in terms of field component along the θ direction and $E_{\theta, ERT}^{(i)}(\theta, \phi)$ is the field component of the received ray obtained from FASANT simulation.

$$E_\phi^{(i)}(\theta, \phi) = E_{\phi, ERT}^{(i)}(\theta, \phi) A_\phi(\theta, \phi) \tag{4.2}$$

where $A_\phi(\theta, \phi)$ is the far field radiation pattern of the antenna in terms of field component along ϕ direction and $E_{\phi, ERT}^{(i)}(\theta, \phi)$ is the field component of the received ray obtained from FASANT simulation.

The channel response for a SISO link between transmitter m and receiver n, dropping the angle of arrival for notational convenience is then:

$$h_{m,n}(t, \tau) = \sum_{i=1}^{N} E_\theta^{(i)}(t)\delta(t - \tau_i) + E_\phi^{(i)}(t)\delta(t - \tau_i) \tag{4.3}$$

The MIMO channel, $\widetilde{\mathbf{H}}_C$, is formed from these SISO links as in Equation 2.9. It is important to note that this channel model takes into account mutual coupling by using the radiation patterns simulated in the presence of mutual coupling. This channel response was calculated at each of the 14 frequency bands, by running a simulation at each center frequency. In this way, 14 $\widetilde{\mathbf{H}}_{C,band}$'s are formed.

4.1.1 Lab Model

A 3-dimensional model of the the DWSL lab room was created for the purpose of these simulations. This is Room 325 of Drexel University's Bossone building. The model takes into account all of the major features in the environment including cubicle partitions, desks, the walls, supporting column, and floor of the room. While this model is a fair representation of the environment, it does not include all of the actual features. For example, chairs and computers were ignored. These objects will cause additional scatterings and reflections in the actual environment. However, the rays affected by these elements will likely have insignificant power compared to the those scattered and reflected over the major environmental features. This will be discussed further in Chapter 5 where the simulation is validated. The model is shown in Figure 4.1. The results from one link in the FASANT simulation is shown in Figure 4.2. From this figure it is clear that there is a very large amount of multi-path components in an UWB link. It is also clear that the multipath components impinge on the receiver from all directions.

4.1.2 Link Setup

Two transmitter locations and ten receiver locations were chosen for a total of twenty different links. These locations were arbitrarily chosen to provide receivers with rich local scattering environments (RLSE) and poor local scattering environments (PLSE). Table 4.1 lists which links have RLSE and which have PLSE. Simulations were done at each link at each of the 14 sub-band frequencies with a total of ten antenna spacings ranging from 0.1λ to λ in increments of 0.1λ, where λ corresponds to the wavelength at 3.168 GHz, or 8.74 centimeters. The location of the antennas are shown in Figure 4.3.
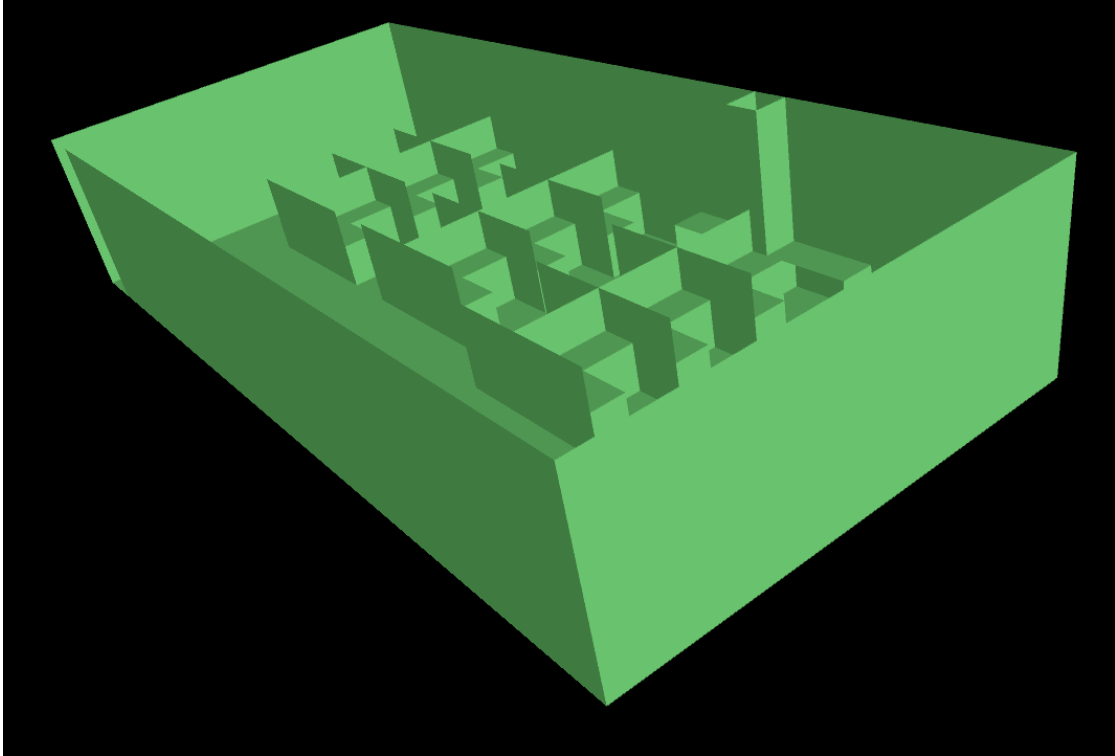
Figure 4.1: 3-dimensional model of the DWSL

Scenario	Receiver Number
Receivers with RLSE	3, 4, 5 ,6 7
Receivers with PLSE	1, 2, 8, 9, 10

Table 4.1: Link Scenarios

4.2   Result Analysis

4.2.1   Channel Impulse Response

The impulse response of the UWB channel is examined at various frequency bands in order to demonstrate the need to simulate at each of the frequency bands. Figure 4.4 shows the impulse response in a RLSE scenario, transmitter 2 to receiver 5, at the 1st and 14th frequency bands. Figure 4.5 shows the impulse response in a PLSE
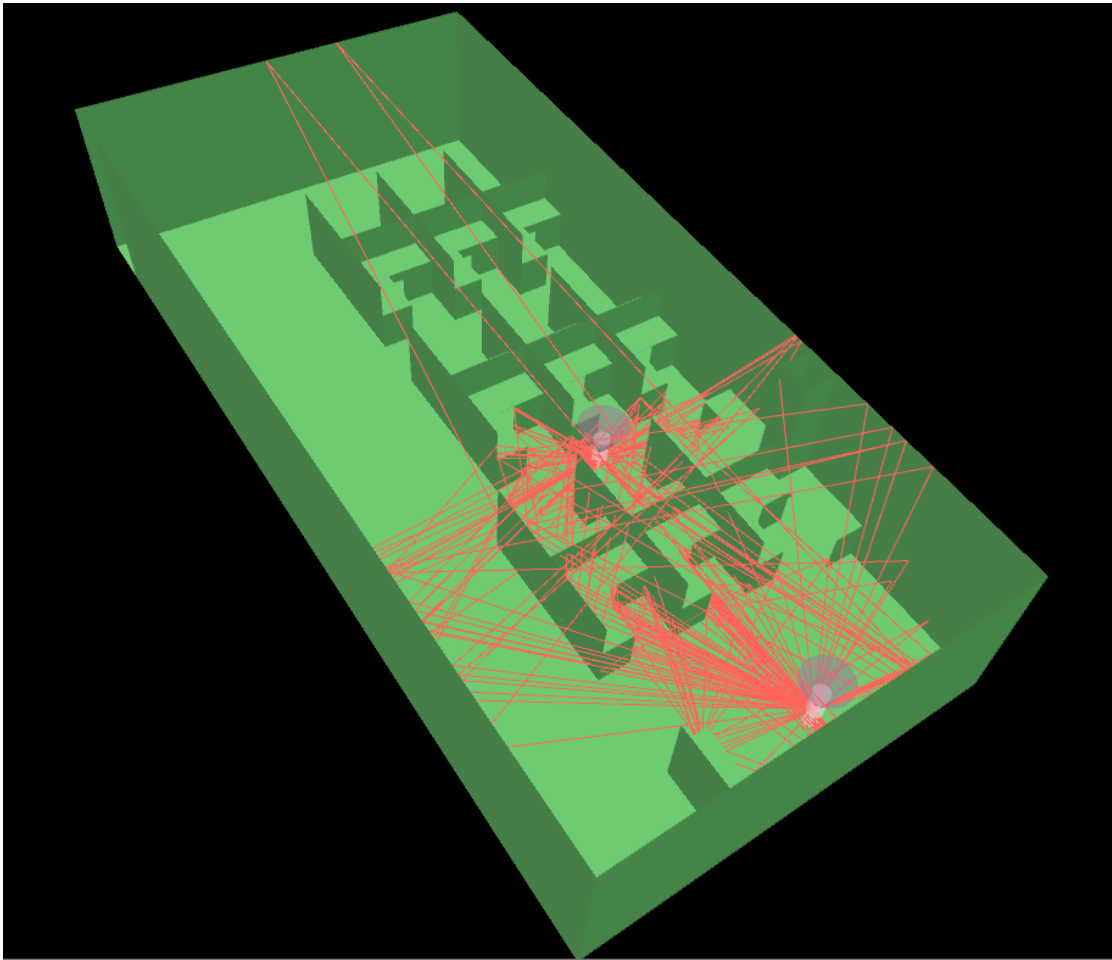
Figure 4.2: DWSL Simulated Link with multipath components displayed

scenario, transmitter 1 to receiver 1, at the 1st and 14th frequency bands. It is important to note that the impulse response of the 14th band is not just a shifted and scaled version of the impulse response of the 1st band. Therefore, a method which would simulate at one frequency and then extrapolate the data to other frequencies (as used successfully in [18] would not work for this simulation. This is caused by the the frequency selectiveness of the materials in the environment. This frequency selectiveness is not linear and therefore unsuited for extrapolation. For example, some materials in the environment will block higher frequency components better than low

Figure 4.3: DWSL Simulated Link Setup

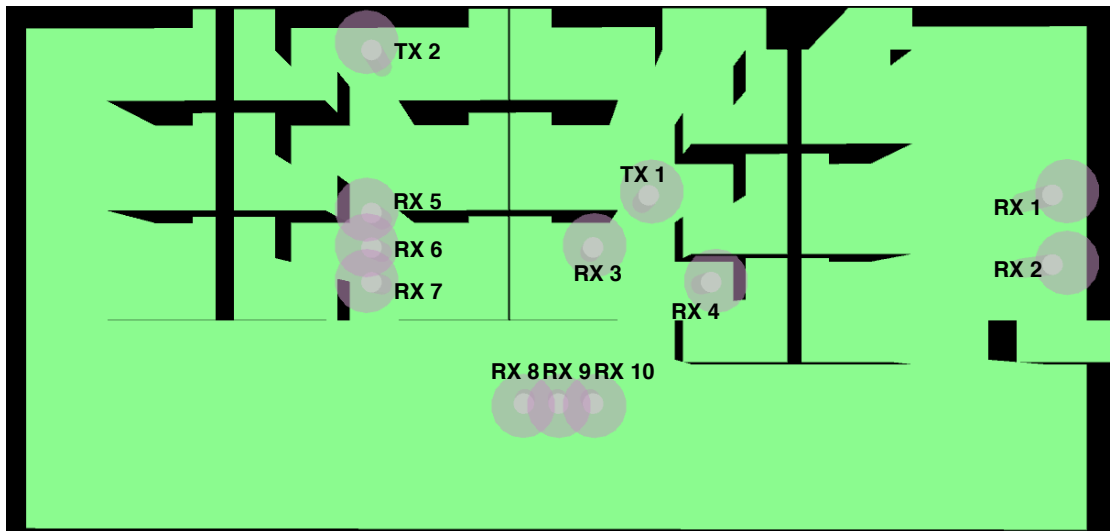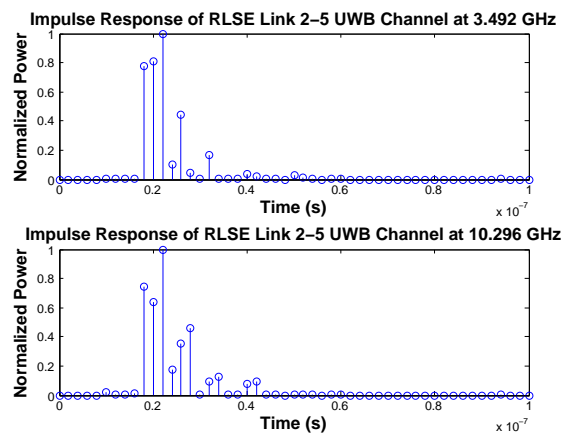frequency components.

Figure 4.4: Impulse Response of Link 2-5 (RLSE) UWB Channel at varying frequency
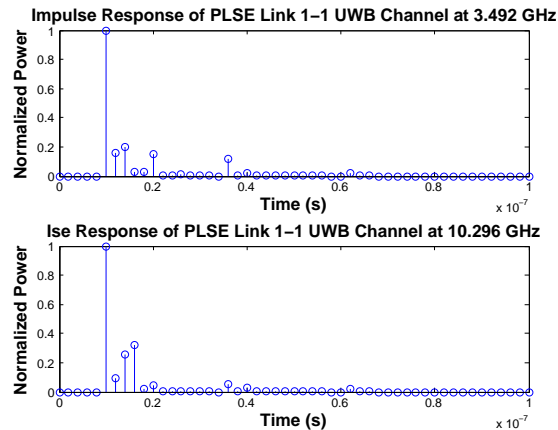
Figure 4.5: Impulse Response of Link 1-1 (PLSE) UWB Channel at varying frequency

4.2.2 Ray Types

To gain a better understanding of the MIMO-UWB channel, the types of rays received are examined. As mentioned in Section 4.1, FASANT detects rays propagating through seven different modes of propagation mechanisms: direct, reflected, diffracted, double reflected, reflected-diffracted, diffracted-reflected and diffracted-diffracted. The average number of rays of each type over all RLSE and PLSE scenarios are shown in Table 4.2. The dominant method of propagation is diffracted-diffracted. This implies that there are a lot of scatterers in the environment. While most of these diffracted-diffracted rays are low power, their total contribution to the signal strength is not negligible.

4.3 Spatial Correlation

The spatial correlation between adjacent paths is given in Equation 2.17. The spatial correlation is a measure of similarity between adjacent channels. Ideally, the channels would be completely independent, allowing much more information to be

Ray Type	Number in RLSE Link	Number in PLSE Link
Direct	1	0
Reflected	2	0
Diffracted	16	7
Double Reflected	5	0
Reflected-Diffracted	51	12
Diffracted-Reflected	46	18
Double Diffracted	244	156

Table 4.2: Ray Types

Figure 4.6: Simple case illustrating effect of antenna gain in spatial correlation

exchanged. When channels are not completely independent, some of the information sent over them is the same.

Since the antennas are spatially near each other, they see the local environment the same way. Scatterers and reflectors in the environment affect each antenna similarly. As demonstrated in Figure 2.1, the relationship between the wavelength of a ray and the physical distance between antennas is very important in the spatial correlation in

Figure 4.7: Simple case illustrating effect of antenna gain in spatial correlation

between elements. Additionally, the way the gain of the antenna effects the received signal will affect the spatial correlation. Figure 2.1 assumes the radiation patterns of each of the antennas is the same. However, when mutual coupling is considered, this is not the case. Another simple example is illustrated in Figure 4.6. In this case, the antennas have the same radiation pattern. They both receive the same exact ray, since they are not spatially separated along the direction the ray travels.

Now, if for instance, the radiation patterns of the two antennas were different, as is the case when considering mutual coupling, a scenario like that shown in Figure 4.7 could arise. In this case, the radiation pattern of the rightmost antenna has 6 dB of gain over the leftmost antenna at this particular angle of arrival. In this case, the two rays are not identical as they were in Figure 4.6 even though they are not spatially separated along the direction the ray travels. The interference caused by this ray will be more substantial for the rightmost antenna than the leftmost one.

The spatial correlation between antennas is also highly dependent on the distance between the antennas relative to the wavelength of the received rays as discussed

in Section 2.4.1. As the wavelength is different for each UWB frequency band, it is unlikely that the spatial correlation between antennas will be constant over frequency. Figures 4.8 and 4.9 show the spatial correlation at element separations of 0.1λ and 0.5λ where λ is once again 8.74 centimeters, corresponding to the first frequency band of 3.432 GHz. Figure 4.8 takes the average of all RLSE scenarios in Table 4.1. Figure 4.9 takes the average of all PLSE scenarios in Table 4.1.

At a separation of 0.1λ, mutual coupling decorrelated the channels to each receiving element by an average of 0.21 in the RLSE case and 0.42 in the PLSE case. At a separation of 0.5λ, mutual coupling decorrelated the channels to each receiving element by an average of 0.09 in the RLSE case and 0.16 in the PLSE case. The degree of decorrelation caused by mutual coupling is higher in the PLSE scenarios. Additionally, the effects of mutual coupling are more pronounced at closer antenna spacings.

As multi-band UWB is supposed to use pseudo-random frequency hopping [10], it is of interest to note the decorrelating effect of mutual coupling when averaged over all frequency bands. If we average the spatial correlation over all frequency bands (see Figures 4.10 and 4.11), we find that in general the effects of mutual coupling decorrelate adjacent channels. In RLSE scenarios, mutual coupling decorrealted adjacent channels by an average of 0.13. In PLSE scenarios, mutual coupling decorrealted adjacent channels by an average of 0.20. This is different than the narrowband case where mutual coupling increased the spatial correlation in PLSE scenarios [6]. The receivers which have poor local scattering environments are affected more by mutual coupling.
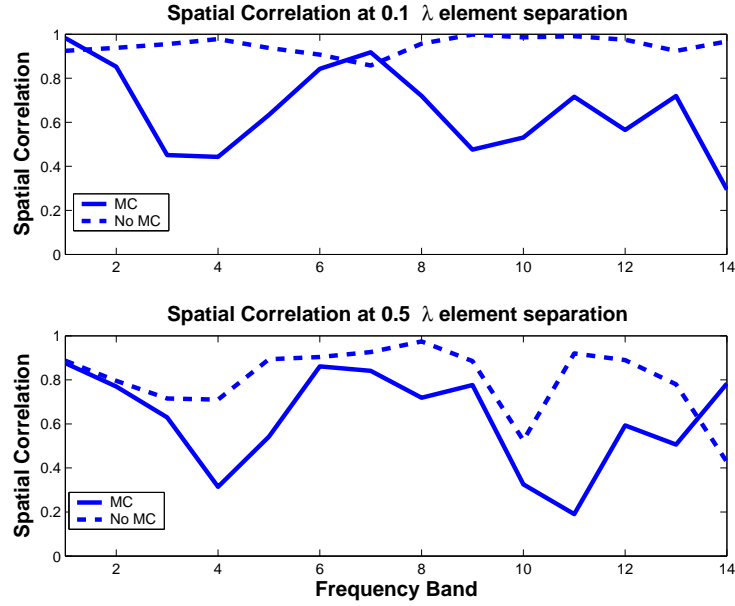
Figure 4.8: Spatial Correlation of RLSE scenario at different element separations

4.4 Capacities

In order to study the capacities achieved in the simulation, the results must be normalized. The normalization factor, η, is given in Equation 4.4 This normalization mitigates the effects of path loss between the various links. This normalization effectively sets the channel gain to unity. This allows us to apply an arbitrarily chosen received signal-to-noise ratio to the results.

$\mathbf{H}_{C,band}$ denotes channel responses computed via Equations 4.1 and 4.2 using antenna radiation patterns that account for mutual coupling and $\mathbf{H}_{NoC,band}$ denotes channel responses computed using antenna radiation patterns that do not account
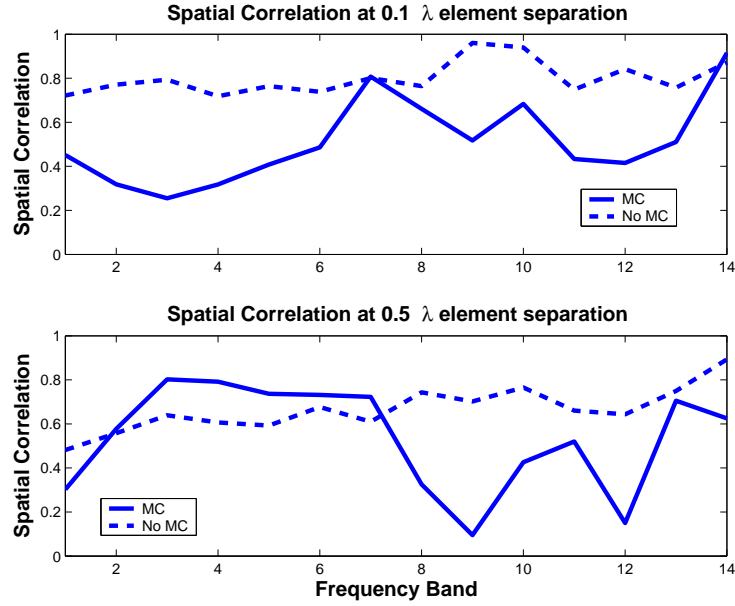
Figure 4.9: Spatial Correlation of PLSE scenario at different element separations

for mutual coupling.

$$\eta = \sqrt{\frac{NM_tM_r}{\sum\limits_{band=1}^{14} ||0.5\widetilde{\mathbf{H}}_{\mathbf{C,band}}||_F^2 + 0.5||\widetilde{\mathbf{H}}_{\mathbf{NoC,band}}||_F^2}} \qquad (4.4)$$

where 14 is the number of frequency bands, and $||\mathbf{M}||_F^2$ is the Frobinius norm of matrix $\mathbf{M}$.

As discussed in Chapter 2, three capacities are considered: equal power allocation, water-filling, and beam-forming. These capacities are shown for RLSE links with and

Figure 4.10: Average Spatial Correlation of RLSE scenario over all frequency bands

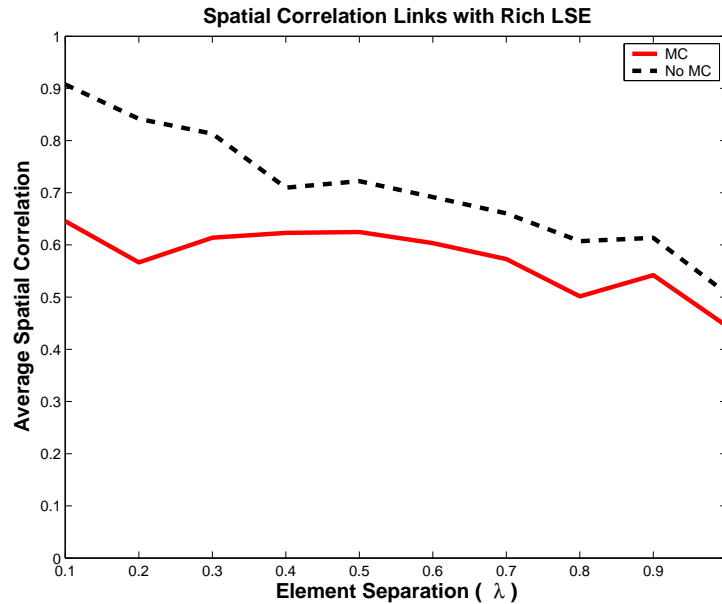without mutual coupling and PLSE links with and without mutual coupling. A SNR of 12 dB is considered nominal [10] and is used for all cases. The antenna element separation is given in terms of λ which is the wavelength at frequency band 1, 3.492 GHz, and is equal to 8.74 centimeters.

4.4.1 Capacity in RLSE

Figure 4.12 takes the average capacity over all RLSE scenarios listed in Table 4.1 as a function of frequency at element separations of 0.1λ and 0.5λ. The capacity without considering mutual coupling is nearly constant and is relatively unaffected as a function frequency. The capacity when mutual coupling is considered varies by as much as 4 bits per second per Hertz. The capacity is not monotonically increasing
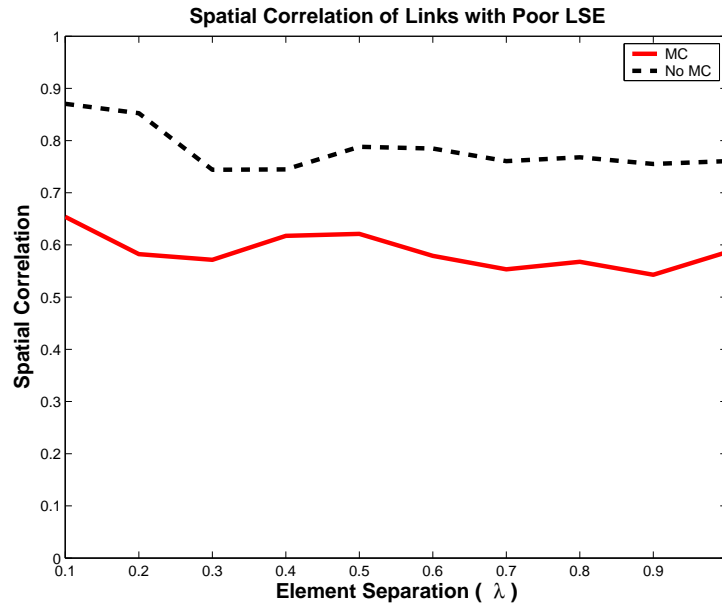
Figure 4.11: Average Spatial Correlation of PLSE scenario over all frequency bands

as a function of frequency, as the spatial correlation is not linearly a function of frequency. Accounting for mutual coupling increases the capacity at almost every element spacing.

Figure 4.13 shows the average capacity over all RLSE scenarios listed in Table 4.1. Beamforming and waterfilling achieve practically the same performance of an average capacity over element separation of 2.6 bits per second per Hertz when mutual coupling is considered. This is a 40% improvement over the case where mutual coupling is not considered. The fact that beamforming and waterfilling achieve approximately the same capacity means that on average, when having a received signal strength of 12 dB, waterfilling determines there is only enough power to send to one eigenmode. Equal power allocation achieved an average capacity of 2.12 bits per second per Hertz
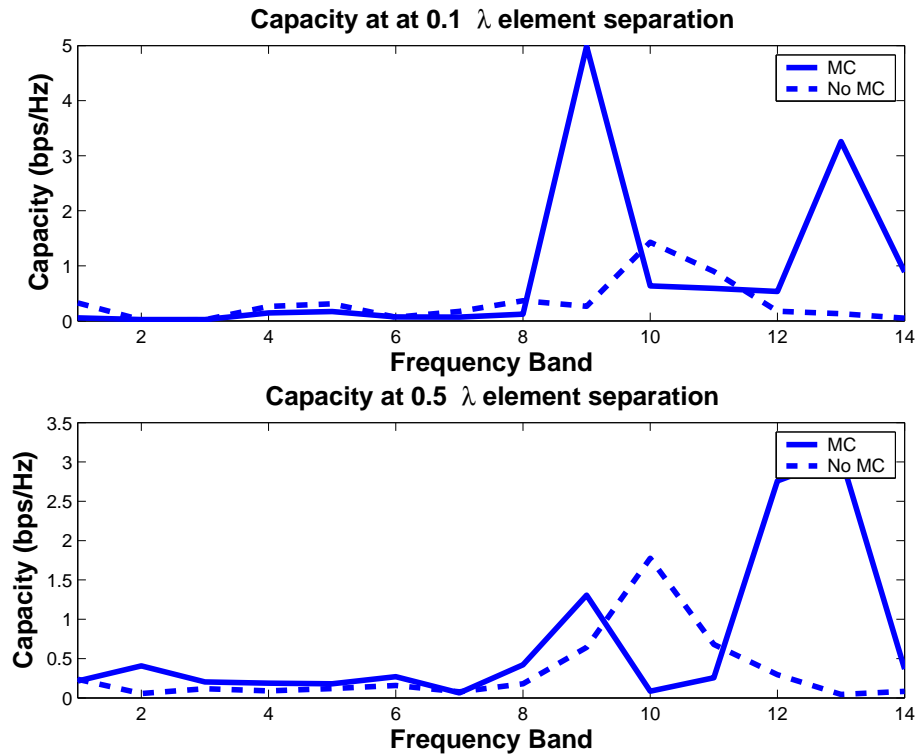
Figure 4.12: Channel Capacity in RLSE over frequency bands

when mutual coupling is considered. This is over a 40% difference than the capacity when mutual coupling is ignored.

4.4.2 Capacity in PLSE

Figure 4.14 takes the average capacity over all PLSE scenarios listed in Table 4.1 as a function of frequency at element separations of 0.1λ and 0.5λ. The capacity without considering mutual coupling is nearly constant and is relatively unaffected as a function frequency. The capacity when mutual coupling is considered varies by as
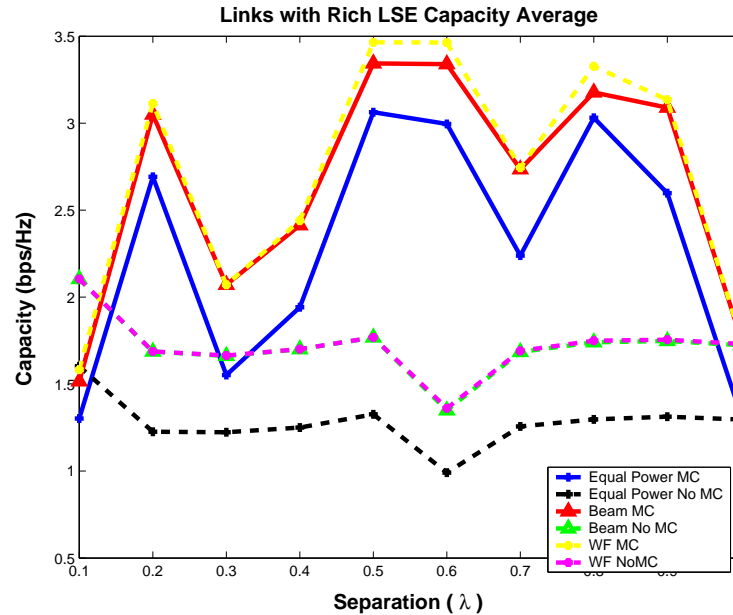
Figure 4.13: Channel Capacity in RLSE over element separation

much as 5 bits per second per Hertz. The capacity is not monotonically increasing as a function of frequency, as the spatial correlation is not linearly a function of frequency. Accounting for mutual coupling changes the capacity at almost every element spacing. This is especially noticeable at the higher frequency bands

Figure 4.15 shows the average capacity over all PLSE scenarios listed in Table 4.1. Beamforming and waterfilling achieve practically the same performance of an average capacity over element separation of 1.9 bits per second per Hertz when mutual coupling is considered. This is a 70% improvement over the case where mutual coupling is not considered. The fact that beamforming and waterfilling achieve approximately the same capacity means that on average, when having a received signal strength of 12 dB, waterfilling determines there is only enough power to send to one eigenmode.
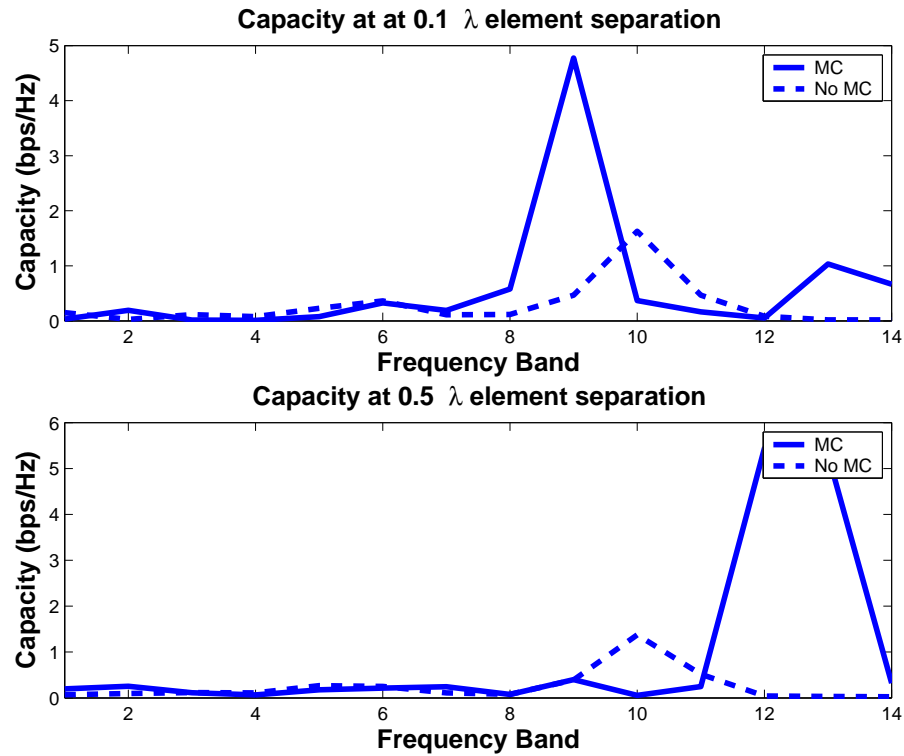
Figure 4.14: Channel Capacity in PLSE over frequency bands

Equal power allocation achieved an average capacity of 1.4 bits per second per Hertz when mutual coupling is considered. This is over a 70% difference than the capacity when mutual coupling is ignored.

4.5 Conclusion

When averaged over all frequency bands, considering mutual coupling resulted in significantly increasing capacity in both PLSE and RLSE scenarios. Additionally, beam-forming and water-filling both significantly outperformed equal power alloca-
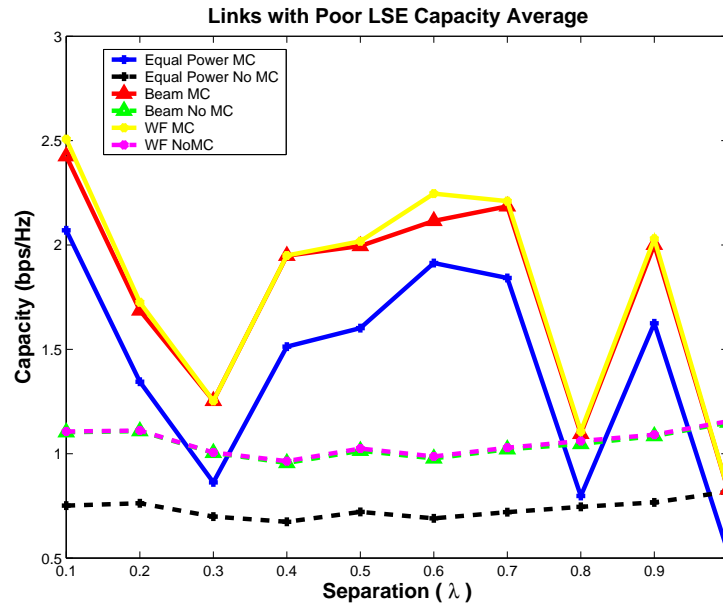
Figure 4.15: Channel Capacity in PLSE over element separation

tion which is expected as they are closed loop techniques. However, the downside of closed loop techniques is increased network overhead to feedback channel information. The overhead capacity for this is not examined in this document. They take advantage of knowledge of the channel, and therefore consider the decorrelation effects of mutual coupling. Of the closed loop techniques, water-filling outperformed beam-forming significantly.

A number of conclusions can be drawn from these results. The fact that capacity was non-monotonic as a function of element separation means that MIMO-UWB systems should be designed with specific dimensions in mind. For example, in a application where there is a rich scattering environment, an antenna element separation of 4.37 centimeters may give the highest capacity (see Figure 4.13). However, if there

was a lack of local scatterers, an antenna element separation of 0.87 centimeters may give the highest capacity (see Figure 4.15). These values are highly dependent on the environment and antennas used, but there is motivation to consider all of these variables before designing a full MIMO-UWB system.

These results also motivate the design of UWB antennas. It is desirable to design antenna array in which mutual coupling has a significant impact on spatial diversity. Additionally, there is very strong evidence that mutual coupling cannot be ignored in UWB MIMO antenna design, as it was demonstrated that even in the most insignificant cases, the capacities achieved when considering mutual coupling differed by 40% from the capacities achieved without considering mutual coupling.

5. Experimental Validation

5.1 Experimental Setup

5.1.1 Hardware

The experimental setup for the channel sounding system that will be used for model validation is based on a network analyzer. We will use the Agilent N52308 network analyzer, from the Drexel Wireless Systems Laboratory. In this experimental system, a signal is generated from one of the ports on the network analyzer, which is connected to an emitting antenna. This propagating RF signal is then detected on receiving antenna, and connected to a receiving port of the network analyzer through a pre-amplifier. This measurement is the S_{12} parameter. A controlling computer handles the network analyzer data acquisition and controls the location of the receiving antenna via custom written Labview Virtual Instruments. The antenna is moved using a TDK Positioning Arm SI-300. As discussed in Chapter 3, the single ended elliptical antenna (SEA) had the best performance of the antennas considered in this work and was used for all the simulations in Chapter 4. Therefore, all measurements were conducted using the fabricated SEA antennas. A block diagram of the hardware is shown in Figure 5.1. The actual equipment is shown in Figure 5.2.

5.1.2 Methodology

There are a plethora of UWB MIMO scenarios to consider when analyzing the UWB channel. Antenna separation, frequency band, antenna geometry, transmitter and receiver location are all variables than can be changed. A measurement campaign to validate all of these would be extremely time-consuming and ultimately unnecessary. We will validate the simulated data at a select few scenarios to prove
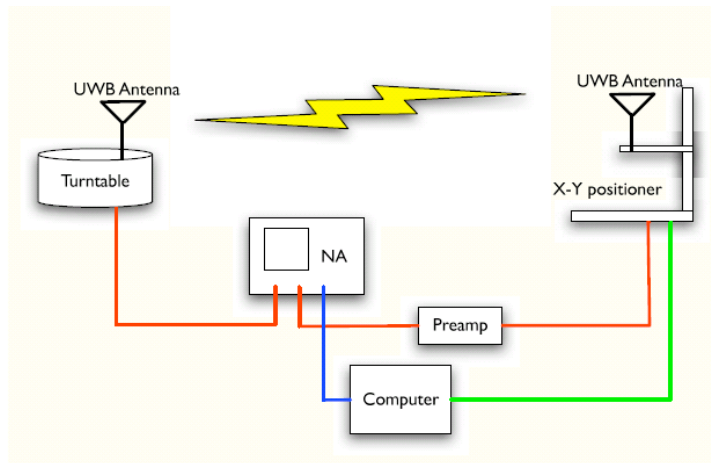
Figure 5.1: Channel Sounder Setup

our simulation methods are valid. Having proven this, we can easily extend our simulations to cover any number of scenarios. The links measured were (from Figure4.3) for PLSE scenarios, transmitter 1 to receivers 1, 2, and 8 and for RLSE scenarios transmitter 2 to receivers 4, 5, and 6. The results show the average over these links. The measurements were made with a 0.5λ separation between elements.

For cases including mutual coupling the link from each transmitter to each receiver was measured using the network analyzer with the non active element at each end terminated by a 50 Ω load. For the no mutual coupling case, the measurements were made for each transmitter to receiver element with no other antenna element present. For each location, small spatial perturbations were made and the average S_{12} parameter was taken. Additionally, measurements were done at each frequency band and samples were averaged over 75 time snapshots. The power amplifier used is flat over the frequency range of 1 GHz - 8 GHz. The power amplifier cannot be included in the network analyzer calibration procedure, so the collected data is only valid for the first 9 UWB frequency bands (3.492 GHz - 7.656 GHz).
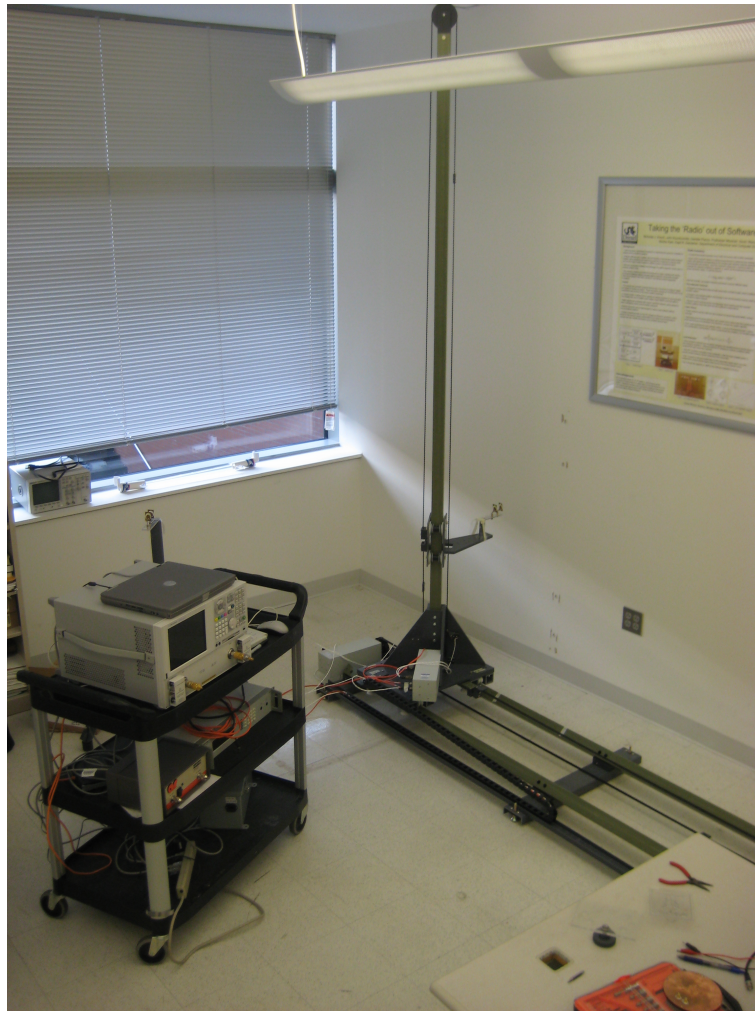
Figure 5.2: Actual Channel Sounder Setup

5.1.3 Results
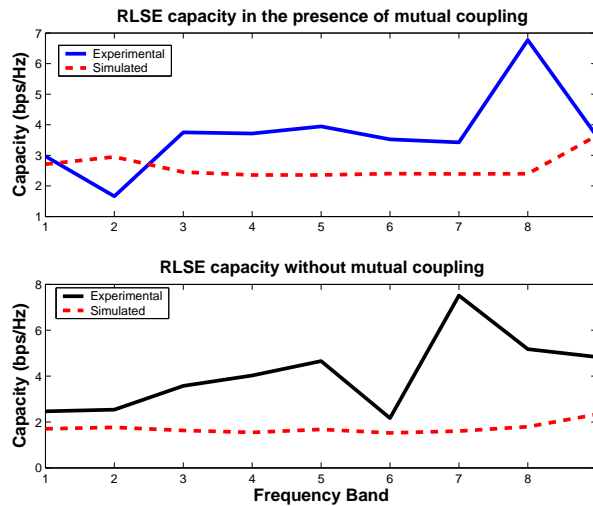
Figure 5.3: Measurement vs. Simulation in RLSE scenarios

The **H** matrices measured are normalized via the same method as in Section 4.4. As the ERT model does not include all actual objects in the environment, perfect correlation is not expected between the simulated and actual results. Connectors, cables, and other environmental factors also have a negative impact on performance. The measurements in the PLSE scenario (Figure 5.4) closely match the simulation results. There is a large discrepancy in the RLSE scenario (Figure 5.3). This error is contributed to the FASANT simulation set up. There is an abundance of multi-path component, the majority of which are the results of diffraction and reflections in the local environment. These reflections and diffractions are highly dependent on
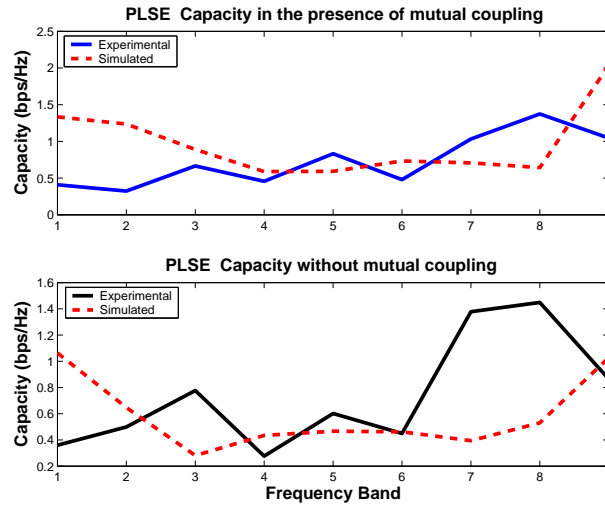
Figure 5.4: Measurement vs. Simulation in PLSE scenarios

the materials in the environment. As the FASANT simulation uses a simplified environmental model with a limited number of materials, the diffractions and reflections are expected to be different. This suggests that a more complete, accurate model should be used when modeling UWB channels using electromagnetic ray tracing. It is important to note that the measurements agree with the simulation in the fact that the RLSE scenarios achieve a much greater capacity than the PLOSE scenarios. This shows that the RLSE MIMO-UWB environment displays high spatial diversity in both simulation and real-life environments.

6. Conclusion and Future Research

6.1 Conclusion

This thesis provides a comprehensive study of the effects of mutual coupling in UWB MIMO systems. A UWB MIMO model was introduced in Chapter 2. Chapter 3 introduced several UWB antennas. Two geometries were developed, fabricated, and tested. Chapter 4 described the computational electromagnetics used to study the effects of mutual coupling in the UWB MIMO system and Chapter 5 validated a subset of the simulations using a channel sounding experiment. In all cases considered, accounting for mutual coupling actually increased capacity in both open and closed loop systems. This is contrary to the narrowband case where mutual coupling only increases capacity in LOS scenarios. This is because in the UWB system, the spatial correlation between adjacent channels is generally decreased by mutual coupling. This is due to the high number of multipath components, the differences in antenna radiation patterns due to mutual coupling, and the different frequency bands in the MIMO-UWB system. Since the antenna positions are fixed in a system, the distance between antennas in terms of wavelength changes with frequency. This has an impact on spatial correlation as demonstrated in Section 2.4.1. While considering mutual coupling will not guarantee less spatial correlation at every frequency band and at every possible antenna separation, it was shown that on average it will in Section 4.3. Additionally, it was shown in Section 4.4 that by using closed loop capacity techniques, namely waterfilling, to take advantage of this decorrelation great increases in capacity could be made in the MIMO-UWB system. While there is no definitive UWB MIMO statistical model, an adaptation to the Kronecker model has been proposed in literature [19]. However, the mutual coupling between elements is

ignored. By considering mutual coupling at each end of the channel, a much more realistic model can be made.

6.2 Future Research

UWB systems are still relatively new and cutting edge. As the required hardware becomes cheaper, more and more WPAN will adopt UWB as their standard form of communication. This study shows that improvements in capacity can be made by considering the entire system, including the antennas and antenna element separation, during design. Antenna elements can be placed very close together and actually improve performance. There is also now motivation to design antennas with the interest of causing a high degree of mutual coupling in arrays. Normally, the intent in antenna design is to minimize mutual couping. Additionally, there is promise for even greater capacities by designing smart systems that take advantage of channel knowledge to increase capacity. However, achieving these high capacities will require the development of low overhead channel information techniques. MIMO-UWB systems have great potential to reach very high data rates for use in WPAN environments.

Bibliography

[1] *FASANT(dll version) user's guide.*

[2] *Fractus FR05-S1-P-0-107 Datasheet*, Tech. report, Fractus, 2007.

[3] *HFSS Datasheet*, Tech. report, Ansoft Corporation, 2007.

[4] H. Bölcskei, D. Gesbert, and A. Paulraj, *On the capacity of OFDM based spatial multiplexing systems*, IEEE Transactions on Communications **50** (2002), no. 2, 225–234.

[5] D. Cassioli, M. Win, and A. Molisch, *The ultra-wide bandwidth indoor channel: From statistical model to simulations*, IEEE Journal on Selected Areas in Communications **20** (2002), no. 6, 1247–1257.

[6] B. Clerckx, D. Vanhoenacker-Janvier, C. Oestges, and L. Vanderdorpe, *Mutual coupling effects on the channel capacity and the space-time processing of MIMO communication systems*, Communications, 2003. ICC'03. IEEE International Conference on **4** (2003).

[7] T. M. Cover and J. A. Thomas, *Elements of information theory*, 1 ed., ch. 10, John Wiley and Sons, Inc, 1928.

[8] R. Dragone, J. Kountouriotis, P. Mookiah, and K. R. Dandekar, *Modeling MIMO-UWB OFDM systems with computational electromagnetics*, Global Telecommunications Conference, 2007. GLOBECOM '07. IEEE (Washington, DC), November 2007, pp. 4527–4531.

[9] J. Dyson, *The equiangular spiral antenna*, Antennas and Propagation, IEEE Transactions on [legacy, pre-1988] **7** (1959), no. 2, 181–187.

[10] ECMA International, *High rate ultra wideband PHY and MAC standard*, 1st ed., 2005.

[11] F. Edalat, J. K. Tan, K. M. Nguyen, Nir Matalon, and Charles G. Sodini, *Measured data rate from adaptive modulation in wideband OFDM systems*, 2006 IEEE International Conference on Ultra-Wideband (2006), 195–200.

[12] FCC, *Revision of part 15 of the commission's rules regarding ultra-wideband transmission systems*, 2002.

[13] P. N. Fletcher, M. Dean, and A. R. Nix, *Mutual coupling in multi-element array antennas and its influence on MIMO channel capacity*, Electronics Letters **39** (2003), 342–344.

[14] G. Foschini and M. Gans, *On limits of wireless communication in a fading environment when using multiple antennas*, Wireless Personal Comm. **6** (1998), no. 3, 311–335.

[15] I. Gupta and A. Ksienski, *Effect of mutual coupling on the performance of adaptive arrays*, Antennas and Propagation, IEEE Transactions on [legacy, pre-1988] **31** (1983), no. 5, 785–791.

[16] N. J. Kirsch and K. R. Dandekar, *Modeling effects of mutual coupling considered at both ends of a MIMO channel using computational electromagnetics*, Vehicular Technology Conference, 2004. VTC2004-Fall. 2004 IEEE 60th, vol. 6, September 2004, pp. 4352–4355.

[17] J. D. Kraus, *Antennas*, 2 ed., ch. 15, McGraw-Hill, Inc., 1988.

[18] C. Liang and K. R. Dandekar, *Modeling MIMO-OFDM ad-hoc communication systems with computational electromagnetics*, **6** (2004), 4340–4344.

[19] Z. Lin, X. Peng, K.B. Png, and F. Chin, *Kronecker Modelling for Correlated Shadowing in UWB MIMO Channels*, Wireless Communications and Networking Conference, 2007. WCNC 2007. IEEE (2007), 1583–1587.

[20] W. Q. Malik and D. J. Edwards, *Measured MIMO capacity and diversity gain with spatial and polar arrays in ultrawideband channels*, IEEE Transactions on Communications **55** (2007), no. 12, 2361–2370.

[21] A. F. Molisch, *Wireless communications*, 1 ed., ch. 9, John Wiley and Sons Ltd, 2005.

[22] A. F. Molisch, D. Cassioli, C. Chong, S. Emami, A. Fort, B. Kannan, J. Karedal, J. Kunisch, H. G. Schantz, K. Siwiak, and M.Z Win, *A compreshensive standardized model for ultrawideband propagation channels*, IEEE Transactions on Antennas and Propagation **5** (2006), no. 1, 3151–3166.

[23] A.F. Molisch, J.R. Foerster, and M. Pendergrass, *Channel models for ultrawideband personal area networks*, Wireless Communications, IEEE [see also IEEE Personal Communications] **10** (2003), no. 6, 14–21.

[24] B. Mondal and RW Heath Jr, *Adaptive feedback for MIMO beamforming systems*, Signal Processing Advances in Wireless Communications, 2004 IEEE 5th Workshop on (2004), 213–217.

[25] Y. Mushiake, *The input impedances of slit antennas*, IEE of Japan. **69** (1949), no. 3, 87–88.

[26] M. K. Ozdemir, H. Arslan, and E. Arvas, *Mutual coupling effect in multiantenna wireless communication systems*, Global Telecommunications Conference, 2003. GLOBECOM '03. IEEE, vol. 2, December 2003, pp. 829–833.

[27] A. Paulraj, R. Nabar, and D. Gore, *Introduction to Space-Time Wireless Communications*, Cambridge University Press, 2003.

[28] J. Perez, F. Saez de Adana, O. Gutierrez, I. Gonzalez, M.F. Catedra, I. Montiel, and J. Guzman, *FASANT: fast computer tool for the analysis of on-board antennas*, Antennas and Propagation Magazine, IEEE **41** (1999), 94–98.

[29] D. Piazza, N. J. Kirsch, A. Forenza, R. W. Heath, and K. R. Dandekar, *Design and evaluation of a reconfigurable antenna array for MIMO systems*, IEEE Transactions on Antennas and Propagation **56** (2008), no. 3, 869–881.

[30] J. Powell, *Antenna Design for Ultra Wideband Radio*, Ph.D. thesis, Massachusetts Institute of Technology, 2001.

[31] J. Powell, A. Chandrakasan, and C. MIT, *Differential and single ended elliptical antennas for 3.1-10.6 GHz ultra wideband communication*, Antennas and Propagation Society International Symposium, 2004. IEEE **3** (2004).

[32] D. M. Pozar, *Microwave engineering*, 3 ed., John Wiley and Sons, Inc., 2005.

[33] A. Rajagopalan, G. Gupta, A. S. Konanur, B. Hughes, and G. Lazzi, *Increasing channel capacity of an ultrawideband MIMO system using vector antennas*, IEEE Transactions on Antennas and Propagation **55** (2007), no. 10, 2880–2887.

[34] V. H. Rumsey, *Frequency independent antennas*, 1 ed., Academic Press, 1966.

[35] T. Svantesson and A. Ranheim, *Mutual coupling effects on the capacity of multi-element antenna systems*, Acoustics, Speech, and Signal Processing, 2001. Proceedings. (ICASSP '01). 2001 IEEE International Conference on (Salt Lake City, UT), vol. 4, May 2001, pp. 2485–2488.

[36] J. Wang, G. Zhu, and J. Jin, *Optimal power allocation for space-time coded OFDM UWB systems*, 2005 International Conference on Wireless Communications, Networking, and Mobile Computing **1** (2005), 189–192.

[37] M. Yanagi, S. Kurashima, T. Arita, and T. Kobayashi, *A planar UWB monopole antenna formed on a printed circuit board*, Fujitsu Component Limited, 2004.

[38] F. Zheng and T. Kaiser, *On the evaluation of channel capacity of multi-antenna UWB indoor wireless systems*, Spread Spectrum Techniques and Applications, 2004 IEEE Eighth International Symposium on, August/September 2004, pp. 525–529.